

Numerical Simulation of Wave Breaking

VLADIMIR IRISOV

Zel Technologies, LLC, and NOAA, Boulder, Colorado

ALEXANDER VORONOVICH

NOAA/Earth System Research Laboratory/Physical Sciences Division, Boulder, Colorado

(Manuscript received 5 February 2010, in final form 2 September 2010)

ABSTRACT

The wave breaking events in a continuous spectrum of surface gravity waves are investigated numerically in 2D within a framework of the potential motion model. It is claimed that the major physical mechanism leading to wave breaking is “squeezing” of relatively short waves by the surface currents due to longer waves (the “concertina” effect), which causes the shorter waves to steepen and become unstable. It is demonstrated that locations of the breaking events are well correlated with the maximum of local current convergence, although slightly worse correlation of the locations with the local steepness of undulating surface cannot reliably exclude the latter mechanism either. It is found also that the breaking events are very rare for random surfaces with a root-mean-square (RMS) current gradient below a threshold value of about 1 s^{-1} .

The process of wave breaking was investigated by two numerical codes. One of them is based on approximation of continuous media with a discrete Hamiltonian system, which can be integrated in time very efficiently and accurately but is limited to single-valued profiles. The other is the Laplacian approach, which can explicitly exhibit the overturning of plunging breakers. Study of the discrete system shows that wave breaking is associated with the explosive growth of a certain spatially localized mode of the system.

1. Introduction

Breaking waves are an important feature of sea surface dynamics. Discussion of the role they play in different air–sea interaction processes can be found in review papers (Banner and Peregrine 1993; Melville 1996) and in an introductory part of many other papers (see, e.g., Nepf et al. 1998), and we will not repeat it here.

Substantial literature is devoted to both experimental and theoretical investigation of breaking waves. Most of the experimental data are related to tank measurements, although results of the field measurements are also available (see Holthuijsen and Herbers 1986; Weissman et al. 1984; Gemmrich et al. 2008; Gemmrich 2010; Babanin et al. 2007; Banner et al. 2000, 2002). The experimental results demonstrated, in particular, that incipient breaking events of short waves are poorly correlated with local steepness of underlying waves (Holthuijsen and Herbers 1986), wind speed, or wave age (Banner

et al. 2000), although on average there is a correlation between frequency of breaking and significant wave steepness (Banner et al. 2000; Nepf et al. 1998). It was concluded that the intrinsic nonlinearity of the surface waves motion is a dominant reason for breaking with wind forcing playing a secondary role (at least for winds that are not too strong).

The breaking waves can be divided basically into spilling and plunging. The spilling is characterized by small-scale bulge at the crest of breaking waves. It is significantly affected by surface tension, turbulence, and viscosity. Substantial progress, both theoretical and experimental, has been achieved in their description (see the review in Duncan 2001), and they will not be considered in the present work.

Most of the tank work was done by studying repeatable individual breaking waves (the dispersive property of the surface waves was used to focus them onto a selected point along the tank; both kinematic and dynamic features were investigated: Baldock et al. 1996; Bonmarin 1989; Griffin et al. 1996; Nepf et al. 1998; Perlin et al. 1996; Rapp and Melville 1990; Skyner 1996; Stansell and MacFarlane 2002; Wu and Nepf 2002; among others)

Corresponding author address: Vladimir Irisov, NOAA, PSD99, 325 Broadway, Boulder, CO 80305.
E-mail: vladimir.irisov@noaa.gov

and wave breaking caused by developing modulational instability (see, e.g., Babanin et al. 2010); however, experiments with random waves were also made (Caulliez 2002; Ochi and Tsai 1983; Xu et al. 1986). The experiments confirmed that local parameters such as elevation are not good indicators of breaking (Melville and Rapp 1988); spectrum-integrated steepness seems to be more adequate. It was also found that the process of breaking starts at a level of steepness significantly smaller than the critical slope for Stokes waves (Griffin et al. 1996; Perlin et al. 1996; Rapp and Melville 1990). Obviously, breaking waves are always steep at the stage of wave collapse and often it is difficult to separate the beginning of the breaking from subsequent wave overturning. The goal of the paper is to figure out the physical cause of the initial stages of wave steepening.

Theoretical approaches to the problem of wave breaking are obstructed by strong nonlinearity and nonstationarity of the phenomenon, and most theoretical results are obtained with the help of numerical simulations. These were initiated by Longuet-Higgins and Cokelet (1976, 1978) and then followed by many others (Babanin et al. 2007; Banner and Tian 1998; Chalikov and Sheinin 1998, 2005; Dold 1992; Dommermuth et al. 1988; Longuet-Higgins and Dommermuth 1997; Skyner 1996; Song and Banner 2002; Iafrati 2009). Comparison of the results with tank experiments led to the conclusion that the 2D model of the irrotational motion of an ideal fluid provides an accurate description of the nonlinear surface wave motion including an incipient breaking stage (Perlin et al. 1996; Dommermuth et al. 1988; Skyner 1996). [Note that, in Song and Sirviente (2004), Navier–Stokes equations accounting for viscosity and surface tension were also treated numerically.] The 3D effects and turbulence are known to play important role in the later stage of breaking process (Melville 1982, 1996; Nepf et al. 1998; Wu and Nepf 2002; Gemmrich and Farmer 2004; Gemmrich 2010); however, they do not seem to be a prime cause of breaking. Similar to tank experiments, most of the above-mentioned numerical works dealt with individual waves or wave groups. The local instability of the crests of Stokes waves, which commences at steepness slightly less than critical, was established (referred to as “crest” or “superharmonic” instability; MacKay and Saffman 1986; Longuet-Higgins and Cokelet 1978). As early as in Longuet-Higgins and Cokelet (1978), it was noted that Benjamin–Feir modulation instability of wave trains leads to the appearance of individual waves with increased steepness, which can break because of the local instability of the wave crests. Essentially the same mechanism, but with respect to wave spectrum, was advocated recently by Babanin et al. (2007). Works dealing with numerical simulations of

a spectrum of random nonlinear surface waves are rare. We are aware of only one such work (Chalikov and Sheinin 1998, 2005), but it did not consider breaking waves. In spite of many efforts, a complete description of the mechanisms of surface wave breaking under realistic conditions existing in the open sea does not yet exist.

The purpose of the current paper is to present results of numerical Monte Carlo simulations of nonlinear dynamics of 2D, potential, random surface gravity waves which indicate that the dominant physical mechanism causing wave breaking appears to be the “concertina” effect (using the terminology introduced by Longuet-Higgins 1988), which means contraction of waves at the zones of convergence of surface currents. This effect is quite intuitive and also obvious in the geometric optics limit, when the wavenumber of the wave evolves according to the equation

$$\frac{dk}{dt} = -\frac{\partial u}{\partial x}k, \quad (1)$$

where k is wavenumber and u is current velocity; however, the concertina effect holds not only in the geometric optics limit but for an arbitrary wave profile as well (see section 3). Having this specific purpose of the paper in mind, we will not provide a detailed account of the existing literature, limiting ourselves to mentioning the papers that have bearing on the results presented below; for a comprehensive review, we address the interested reader to Banner and Peregrine (1993), Duncan (2001), Longuet-Higgins (1988), and Melville (1996). The main result of our work is that there is a high correlation between locations of breaking events and points with maximal values of the surface current convergence $\Omega = -du/dx$. It was found also that there is a critical value of the convergence, $\Omega_* \approx 1 \text{ s}^{-1}$, below which wave breaking is extremely rare. In section 2, we briefly describe numerical methods used. The main results of the work obtained with the help of Monte Carlo simulations are presented in section 3. Although it is not crucial for the result, it is of interest also to investigate the stability of background motion from the standpoint of evolution of the eigenvalues of its linear perturbations; corresponding study is presented in section 4. Section 5 briefly presents some effects of surface tension that have been studied in the paper only tangentially. Finally, in section 6 we present some comparisons of the threshold value of the current convergence Ω_* with some data available in the literature, and in the concluding section 7 we present a scenario of surface wave breaking following from our results. The appendix is devoted to verifying that the breaking events under consideration are not numerical artifacts.

2. Numerical methods

We have investigated numerically the dynamics of the potential surface waves in a 2D, deep-water, periodic case. The initial conditions are a surface profile and values of the potential at the surface. Two totally independent codes were used.

The first one (“Laplacian” or L-code) is quite traditional. It is based on time stepping following a set of marked fluid particles on the surface (Longuet-Higgins and Cokelet 1976). The crux of the approach is calculation of a linear Dirichlet-to-Neumann (DtN) operator (matrix), which maps values of surface potential at the markers into corresponding values of its normal derivative. Possible deviations from other implementations of our numerical approach are 1) using cubic periodic splines to interpolate the surface profile and surface potential from the marked points onto the whole surface contour and 2) using representation of the potential in terms of distribution of the dipole sources on the surface. Because parametric representation of the surface profile is used, the solution is not restricted to the single-valued profiles and includes overturning. The most time-consuming part is calculation of the influence matrix corresponding to the integral equation with respect to the density of surface dipoles. The solution of corresponding linear equations and time stepping per se is relatively fast. The sawtooth instability characteristic for the method (Dold 1992; Longuet-Higgins and Cokelet 1976) was not observed in our simulations (possibly because of using cubic splines).

Evolution of wave profiles is governed by the equations

$$\begin{aligned}\frac{\partial \mathbf{r}_a}{\partial t} &= \nabla \varphi \\ \frac{\partial \varphi_a}{\partial t} &= \frac{1}{2}(\nabla \varphi)^2 - gh_a + \sigma \kappa_a,\end{aligned}\quad (2)$$

where $\mathbf{r}_a = (x_a, h_a)$ and φ_a are horizontal and vertical coordinates and velocity potential corresponding to a fluid particle on the surface, σ is surface tension, and κ_a is curvature (a is an index marking the particle); $\nabla \varphi$ is calculated at the point $\mathbf{r} = \mathbf{r}_a$. These equations are valid for multi-valued surfaces.

The second code (“Hamiltonian” or H-code) we have used for studying single-valued surfaces solves the Hamiltonian equations

$$\begin{aligned}\frac{dq_i}{dt} &= \frac{\partial H}{\partial p_i} \\ \frac{dp_i}{dt} &= -\frac{\partial H}{\partial q_i}\end{aligned}\quad (3)$$

for the following discrete Hamiltonian:

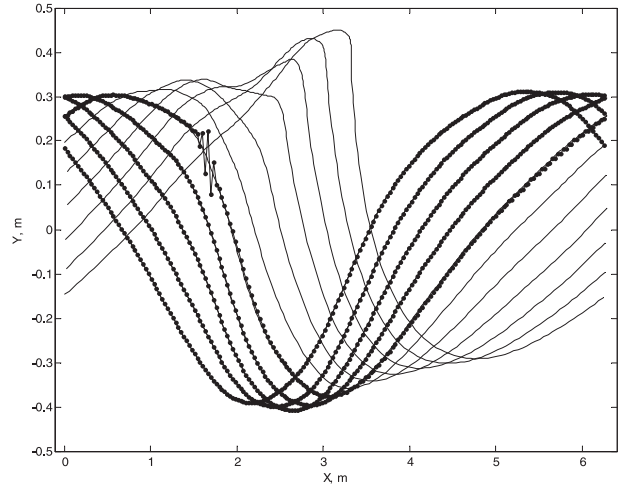


FIG. 1. Surface profile progression calculated with L-code (solid line) and H-code (solid line with dots). Time step between profiles is 0.1 s. The first five profiles calculated by both codes practically coincide with each other except a small area of the last (fifth) H-profile, where high-frequency instability develops. The profile calculated by the L-code shows no short-wave instability at this point, but this area of long wave also shortly becomes steep and unstable.

$$\begin{aligned}H(h, \varphi) &= \frac{1}{2} \sum_{n,m=0}^{N-1} G_{nm} \varphi_n \varphi_m + \frac{g}{2} \sum_{n=0}^{N-1} h_n^2 \\ &+ \sigma \sum_{n=0}^{N-1} \left[\sqrt{1 + \left(\frac{h_{n+1} - h_n}{\Delta x} \right)^2} - 1 \right],\end{aligned}\quad (4)$$

where N is the total number of fixed points $x_n = n\Delta x$ equidistantly distributed along the x axis and the last term represents the surface tension contribution. Here, (h_n, φ_n) are elevation and surface potential at x_n (they are canonically conjugated variables), and the surface profile-dependent matrix $\mathbf{G}_{nm} = \sum_{p=0}^{p_{\max}} \mathbf{G}_{nm}^{(p)}$ represents discrete approximation of the DtN operator, which is expressed as a series in powers of elevations up to a certain finite-order p_{\max} (in our simulation, we used $p_{\max} = 4$). The terms of this series can be calculated recurrently starting from $p = 0$. The nontrivial moment of this approach is to ensure that matrix \mathbf{G} is symmetric and to obtain a discrete analog of the Bernoulli law based on this symmetry. As a result explicit calculation of matrix \mathbf{G} is avoided, and calculation of the right-hand side of the Hamiltonian equations includes only fast Fourier transform (FFT) of vectors (but not matrices) of approximately $N(p_{\max} + 1)$ order. Similar to the L-code, time evolution is accomplished using the fourth-order Runge–Kutta scheme. In contrast to the well-known pseudo-spectral method, where the equations resulting after discretizing corresponding continuous equations are not necessarily Hamiltonian per se, in our approach the

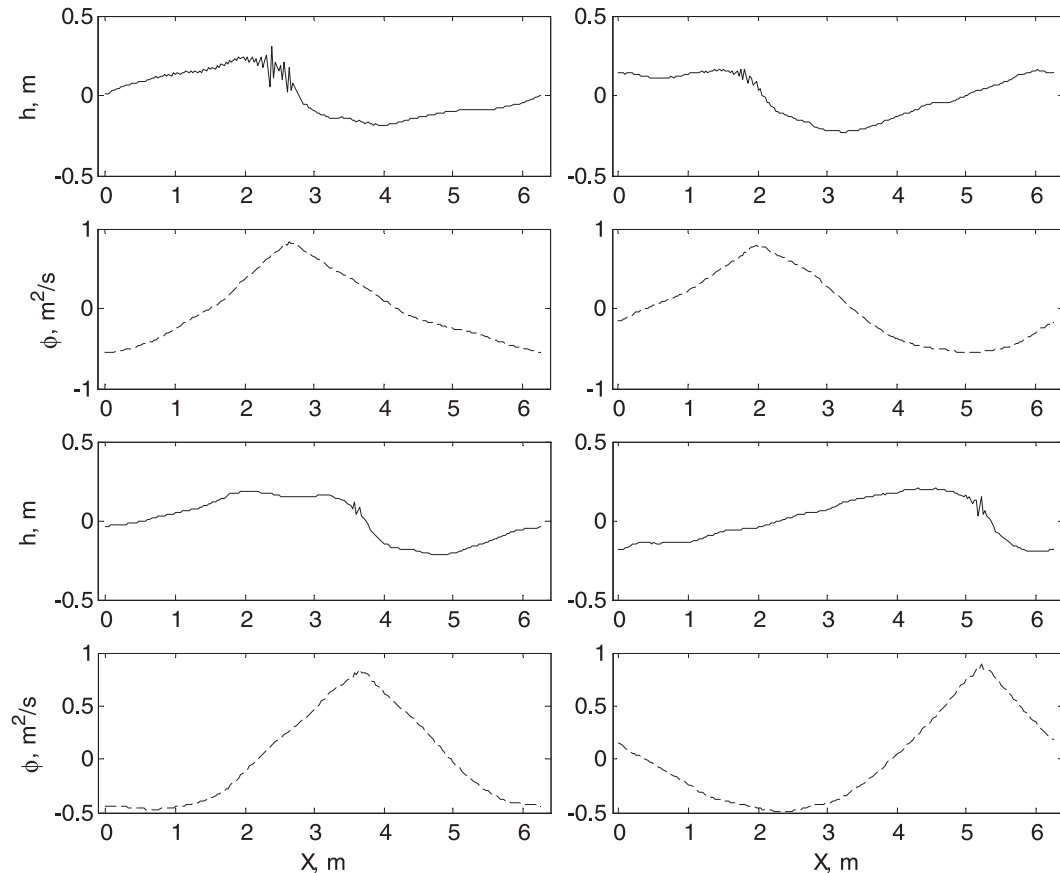


FIG. 2. Four examples of the surface profile (top and third from top) h (solid) and (second from top and bottom) velocity potential ϕ (dashed) at the final stage of instability development.

discrete equations that are solved numerically are explicitly Hamiltonian. In addition to somewhat philosophical preference of approximating the original Hamiltonian system by a simpler system that is also Hamiltonian (so that energy and momentum conservation laws and integral invariants are carried over automatically), another advantage of using explicitly Hamiltonian equations stems from the fact that the linear operator describing evolution of the linear perturbations of the fully nonlinear equations is also Hamiltonian and its spectrum possesses well-known symmetries (see section 4).

Both codes were carefully checked against each other and using conservation laws. Being highly accurate, the L-code is relatively slow, and the bulk of the calculations corresponding to a “benign” stage of wave evolution were done with the help of the H-code, with the L-code being used to accurately calculate stages close to overturning. The comparison of two codes shows that a close proximity between wave profiles is observed up to the incipient overturning. In our simulations, we studied the evolution of a periodic random surface with a period of $L = 6.28$ m and gravity acceleration $g = 9.81$ m s⁻². In

most cases (except for those presented in section 5), capillary effects were neglected, so the results of simulations can be easily scaled. Unless it is stated otherwise, we used $N = 200$ points in the simulations.

In our study, we focused on a random surface. Two different elevation power spectra, $\Phi_k = Ak^{-3}$ and $\Phi_k = Ak^{-4}$, with random phases of constituent harmonics and Gaussian statistics of quadrature components of the elevation spectrum were taken as initial conditions. The $N/2 = 100$ spectral components contained wavenumbers ranging from $k_1 = 1$ m⁻¹ up to $k_2 = 100$ m⁻¹.

The H-code is restricted to single-valued profiles and cannot, of course, describe overturning. However, if the initial root-mean-square (RMS) slope exceeded a certain limit, the solution provided by the H-code demonstrated development of fast-growing local instabilities characterized by high-frequency spatial oscillations. Figure 1 shows time evolution of wave profile calculated by both codes: the solid line corresponds to the L-code and dots correspond to the H-code. One can see that the profiles calculated by both codes practically coincide with each other until the development of oscillations in

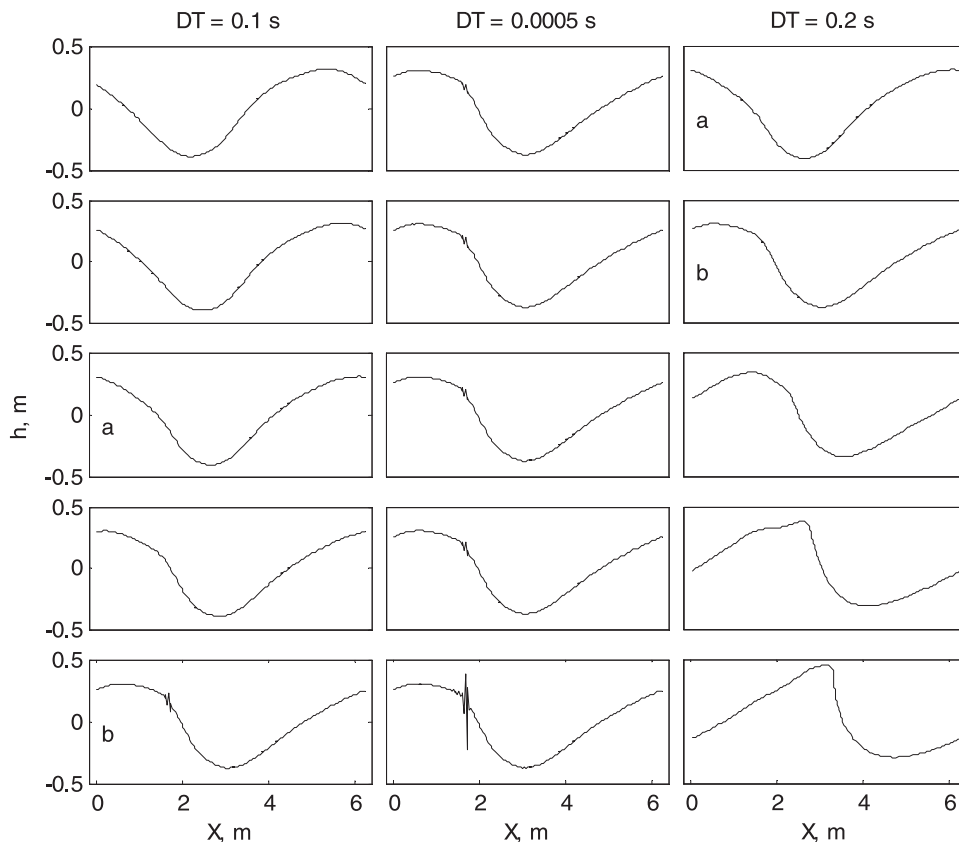


FIG. 3. Surface profile progression with different time steps and numerical codes: (left) H-code 0.1 s, (middle) H-code 0.0005 s, and (right) L-code 0.2 s. Shown in (middle) are the last moments of the instability development; note that the underlying surface can be considered as frozen.

the H-code simulation. Despite such oscillations not describing the process of wave breaking in a continuous medium, we believe that the development of instability is an indication of a locally unstable area of long wave, which ultimately breaks.

Four examples of such instability are shown in Fig. 2 (the initial condition corresponded in these cases to the power spectrum $\sim k^{-4}$ and different sets of random phases of constituting harmonics). It was found (see the appendix) that this instability, developing in the framework of the H-code, is not a numerical artifact and is closely related to the wave breaking calculated by the L-code; for this reason, we will also refer to such events as wave breaking. One can see in Fig. 2 that the instability location appears to be well correlated with the area of surface velocity convergence (minimum or negative maximum of second derivative of velocity potential).

A specific feature of this instability is its extremely fast “explosive” development. Figure 3 shows evolution of the profile, obtained by the H-code, with a time step of 0.1 s (left panels); evolution of the last moments of it with time step of 0.0005 s (middle panels); and evolution of the

same profile, calculated by the L-code (right panels). The starting point of the last time interval with fine time step (top-middle panel) corresponds to a few moments before of the bottom-left panel labeled “b”, so the amplitude of the breaking oscillations is a little less than at the bottom-left panel. One can see that, at the final moments, development of the instability occurs on top of frozen background waves (middle panels). It allows us to consider the instability as explosive (see section 4). Such fast development is quite unusual for numerical instabilities. The L-code demonstrates actual final stage of evolution of the same profile (the left panels labeled a and b correspond to the right panels labeled a and b, respectively), but it results ultimately in overturning of the same part of the surface profile (Fig. 1). This is why we consider H-code breaking as a precursor of wave overturning simulated by the L-code. Analysis of more than 100 random profiles supports this conclusion.

3. Monte Carlo simulations

We generated an ensemble of random surfaces with elevation power spectra $\Phi_k = Ak^{-3}$ and $\Phi_k = Ak^{-4}$ and

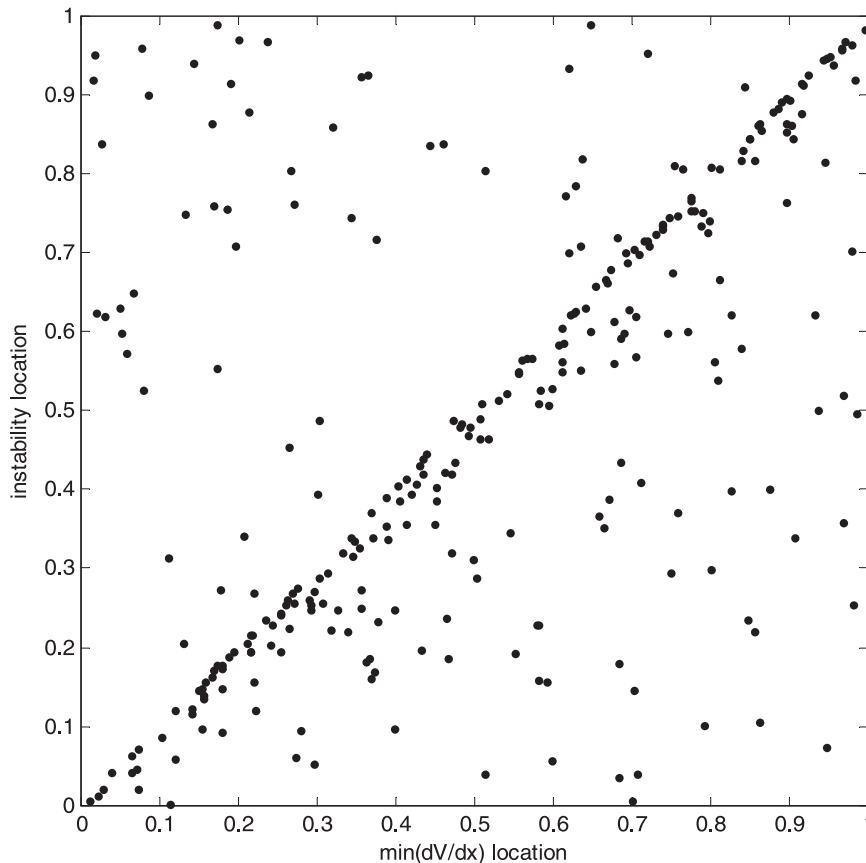


FIG. 4. Correlation between breaker position and the point of strongest current gradient.

studied its time evolution until the first breaking event occurred.

Figure 4 shows the correlation between locations of wave breaking events and the location of the maximum of surface current convergence $-du/dx$. The regression was calculated for the spectrum $\Phi_k = Ak^{-3}$, included 300 realizations, and was calculated as follows: After a breaking event (explosive growth of local high-frequency oscillations) was found by running the H-code, we selected the surface profile calculated 40 time steps prior to the breaking event (each time step was equal to 0.002 s) and suppressed spatial harmonics with an order higher than $n_f = 20$ with the help of $\exp[-0.5(n/n_f)^4]$ low-pass filter. Then the progressive evolution of both the original and smoothed surface profiles was calculated using L-code only. The smoothed surface evolved without wave breaking and remained relatively smooth, whereas the original rough surface exhibited instability characterized by very large local surface curvature. The location of the breaking instability was found as a position of the largest difference between rough and smooth surfaces at the moment of wave breaking, and the location of the strongest current gradient was found from

a solution for the smoothed profile. Taking into account very good agreement between both codes in the absence of instability (Fig. 1), we can say that the H-code, describing discrete Hamiltonian system, was used only for acceleration of the computation, and the final stage of the breaking events was studied by the L-code. It is free from limitations of single-valued surface and finite number of degrees of freedom.

Both the position of the wave breaking event and the position of the strongest current convergence for a particular realization are shown as a scattered plot in Fig. 4 (the locations are normalized on the whole wavelength of 6.28 m). Despite some data scattering, we see quite good correlation with correlation coefficient $C = 0.74$ (we took into account the periodic nature of the problem for calculation of the correlation coefficient). The RMS slope of the initial profile was 0.17, which provides a trade-off between reasonably short computation time and long enough time of the profile evolution before breaking event occurs.

Similar dependence for the spectrum $\Phi_k = Ak^{-4}$ and the same RMS slope is shown in Fig. 5. Note that the data scattering is much less in this case ($C = 0.93$). It is

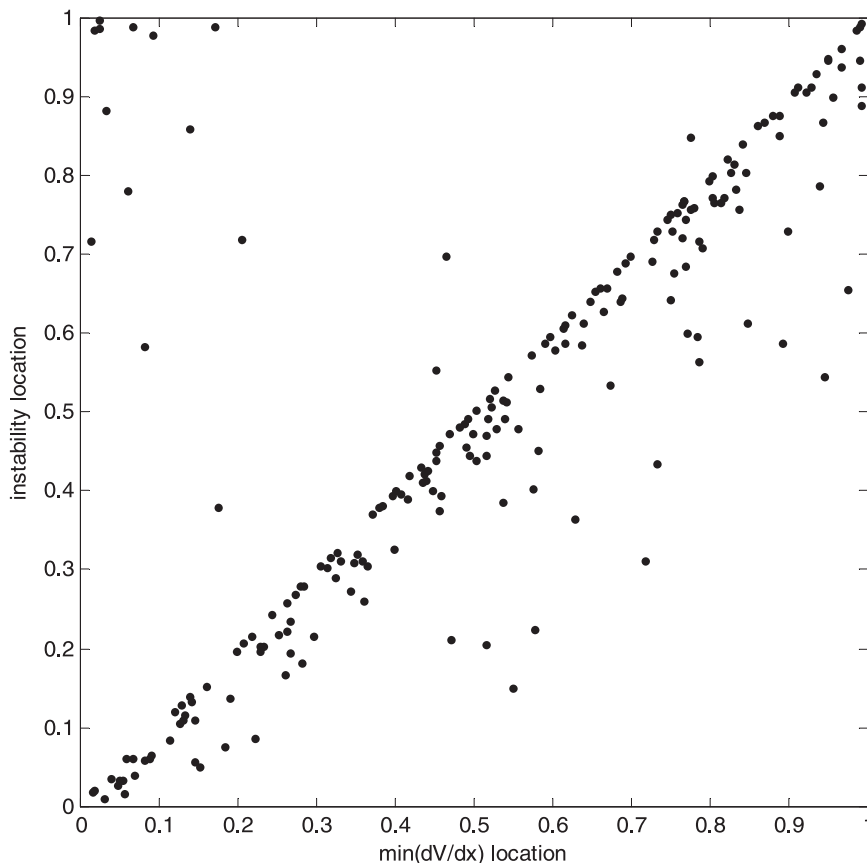


FIG. 5. As in Fig. 4, but for a k^{-4} initial spectrum.

expected because the k^{-3} surface has more local maxima of current convergence as compared to the k^{-4} spectrum, and this obviously results in a poorer correlation between breaking location and position of absolute maximum of current convergence.

However, if one makes the same calculations using the strongest negative slope location instead of current convergence, very similar scatterplots will follow with correlation coefficient $C = 0.74$ for Fig. 4 replaced by a somewhat smaller but close value of $C = 0.73$. This is not surprising, because the correlation coefficient between current convergence and slope is quite high (0.85) for running waves. To determine what physical parameter is related to wave breaking, we calculated similar plots for the spectrum k^{-3} , but with respect to a corresponding statistical ensemble consisting of standing waves. This way, we get better space separation between areas of strong local slope and current gradient. The results are shown in Fig. 6 for slope ($C = 0.70$) and Fig. 7 for current convergence ($C = 0.77$). The difference shows that this is rather current convergence, which causes wave breaking.

The case study in support of this conclusion is shown in Fig. 8, which presents an example of time evolution of

a long standing wave with superimposed on it another standing wave of 30 times shorter wavelength. Initial amplitude of the short wave is 1000 times smaller than the initial amplitude of the long wave (initial condition corresponds to flat surface and two-harmonic distribution of surface potential). The top panel illustrates the evolution of the wave profile, and the bottom panel shows the evolution of high-frequency waves only (the high-frequency profiles are shifted along the y axis). One can see a strong enhancement of ripples at the final stage of wave evolution near the crest of the long wave. This point is characterized by zero slope but maximal value of the surface current convergence. At the next time step, the simulation stops because of dramatic increase of the local curvature.

The equations in (2) for single-valued surfaces are represented in the standard form,

$$\begin{aligned} h_t + h_x \varphi_x &= \varphi_z \\ \varphi_t + \frac{1}{2}(\varphi_x^2 + \varphi_z^2) + gh &= -p. \end{aligned} \quad (5)$$

All values are to be calculated at surface points $x, z = h(x)$. To obtain insight into the origin of the instability

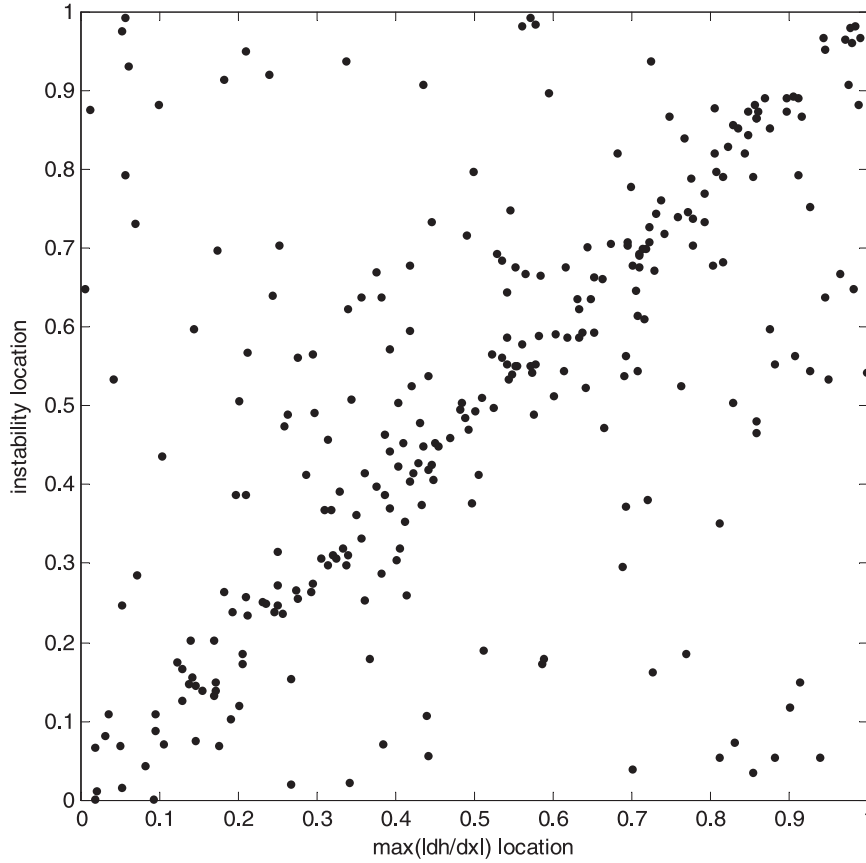


FIG. 6. As in Fig. 4, but for the point of strongest surface slope for standing waves.

going beyond a geometrical-optics consideration, let us linearize (5) with respect to the following time-independent background state:

$$h_0 = 0, \quad \varphi_0 = \frac{\Omega}{2}(z^2 - x^2), \quad p_0 = -\frac{(\Omega x)^2}{2} \quad (6)$$

[surface pressure p_0 is introduced to ensure that (h_0, φ_0) itself is a solution of (5)]. The resulting equations read as

$$\begin{aligned} h_t - \Omega h - \Omega x h_x - \varphi_z &= 0 \\ \varphi_t - \Omega x \varphi_x + g h &= 0, \end{aligned} \quad (7)$$

where all values are calculated at $z = 0$. The equations become simpler in terms of corresponding Fourier transforms $\hat{h}_k, \hat{\varphi}_k$ with respect to x -coordinate $h(x) = \int \hat{h}_k e^{ikx} dk$:

$$\begin{aligned} \frac{\partial}{\partial t} \hat{h}_k - \Omega \hat{h}_k + \Omega \frac{\partial}{\partial k} (k \hat{h}_k) - k \hat{\varphi}_k &= 0 \\ \frac{\partial}{\partial t} \hat{\varphi}_k + \Omega \frac{\partial}{\partial k} (k \hat{\varphi}_k) + g \hat{h}_k &= 0, \end{aligned} \quad (8)$$

where it is assumed that $h(k) = 0$ for $k < 0$. Here it was used that for $k > 0$,

$$(\varphi_z)_k = k \hat{\varphi}_k. \quad (9)$$

One can easily check by inspection that the solution of Eq. (8) is as follows:

$$\begin{aligned} \hat{h}_k &= Z_0 \left(2 \sqrt{\frac{gk}{\Omega^2}} \right) f \left(\frac{g}{\Omega^2} k e^{-\Omega t} \right) \\ \hat{\varphi}_k &= -\sqrt{\frac{g}{k}} \times Z_1 \left(2 \sqrt{\frac{gk}{\Omega^2}} \right) f \left(\frac{g}{\Omega^2} k e^{-\Omega t} \right), \end{aligned} \quad (10)$$

where $Z_{0,1}$ are cylindrical Bessel functions and f is an arbitrary smooth function. The result is quite intuitive and describes the concertina effect of contraction or stretching the perturbation profile by a convergent or divergent current, correspondingly. In particular, if for a certain range of wavenumbers $f \sim k^{-c}$, the perturbation will grow in time as $\exp(c\Omega t)$. Hence, it is natural to expect steepening of short-scale waves in an area of converging surface currents. Because time evolution of the background state is artificially suppressed here by the p_0 term in (6), the solution (10) should be considered as an illustration only.

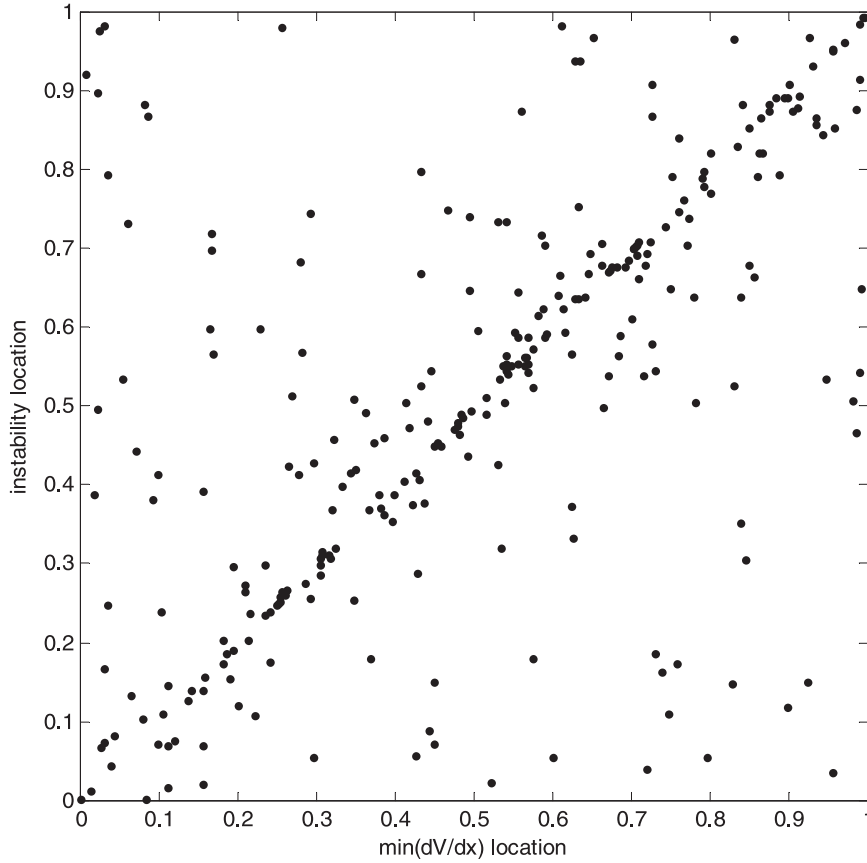


FIG. 7. As in Fig. 4, but for the point of the strongest surface current convergence for standing waves.

4. Normal mode analysis

The results presented in this section refer to the evolution of discrete Hamiltonian system and are not essential for the conclusion drawn in the previous section. However they may be of interest from the point of view of the Hamiltonian system dynamics and provide an insight into the explosive instability we observed.

We study small perturbations of the Hamiltonian equations:

$$\begin{aligned} \frac{d}{dt}\delta q_i &= \sum_k \left(\frac{\partial^2 H}{\partial p_i \partial q_k} \delta q_k + \frac{\partial^2 H}{\partial p_i \partial p_k} \delta p_k \right) \\ \frac{d}{dt}\delta p_i &= - \sum_k \left(\frac{\partial^2 H}{\partial q_i \partial q_k} \delta q_k + \frac{\partial^2 H}{\partial q_i \partial p_k} \delta p_k \right). \end{aligned} \quad (11)$$

These equations are also Hamiltonian; in matrix form they can be rewritten as

$$\dot{\mathbf{z}} = -\mathbf{JSz}, \quad (12)$$

where

$$\mathbf{J} = \begin{pmatrix} 0 & -1 \\ 1 & 0 \end{pmatrix},$$

$$\mathbf{S} = \begin{pmatrix} \frac{\partial^2 H}{\partial q_i \partial q_k} & \frac{\partial^2 H}{\partial q_i \partial p_k} \\ \frac{\partial^2 H}{\partial p_i \partial q_k} & \frac{\partial^2 H}{\partial p_i \partial p_k} \end{pmatrix}, \quad \text{and}$$

$$\mathbf{z} = [\delta q_i; \delta p_i].$$

We can look for eigenfunctions (modes) of the linear problem (11), corresponding to time-independent (frozen) matrix \mathbf{S} , and study evolution of the modes' amplitudes.

Figure 9 shows surface elevation (dashed), velocity potential (dashed-dotted), and the fastest-growing mode for surface elevation (solid) for the case illustrated in Fig. 3. One can easily see that the unstable mode is localized in a small area coinciding with the maximum of current convergence or possibly wave slope. More than 80% of

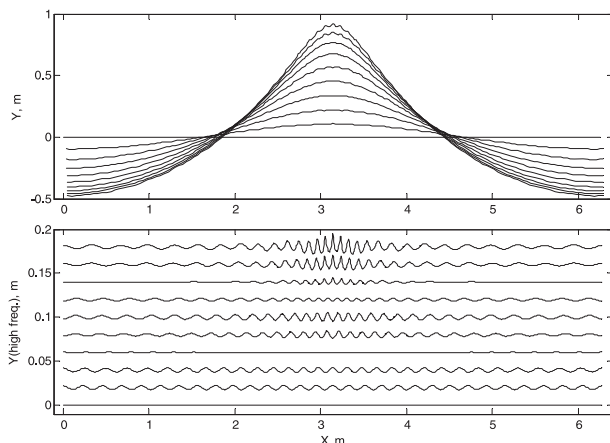


FIG. 8. Evolution of short standing wave superimposed on a long standing wave. (top) Wave profiles and (bottom) high-frequency waves are shown. High-frequency profiles are shifted along the y axis, and time increases from the bottom to the top. Time interval between profiles is 0.05 s, and wavelengths of the long and short waves are correspondingly 6.28 m and $(1/30) \times 6.28$ m. The initial condition was posed as flat surface with periodic undulation of surface current; starting velocity of short wave is 0.001 of the long-wave velocity.

the wave remains smooth and unaffected by the breaking mode. This observation indicates that the condition for the development of instability can be related to some local physical parameters of a large-scale background.

The fixed background state with respect to which linearization (11) is made is selected at a moment of time preceding and close to the moment of explosion.

Figures 10 and 11 show the dependence of the amplitudes of a few fastest-growing modes for the final period of the evolution of the wave shown in Figs. 1, 2, and 9 (Fig. 11 has a finer time scale). Simultaneous evolution of 400 mode amplitudes makes it impossible to trace an individual fastest growing mode until a few final time steps, so we removed most of the 400 modes from Figs. 10 and 11 to make the pictures comprehensible. The fastest-growing mode is clearly prominent among many others with limited amplitudes. This particular mode is shown in Fig. 9 and it is responsible for the “explosion” of the Hamiltonian system; all other modes change insignificantly during the single mode explosion, which justifies frozen background state.

The numerically found dependence of da/dt versus the amplitude a of the fastest-growing mode (see Fig. 11) is shown in Fig. 12. The somewhat unexpected smooth character of the dependence suggests a parabolic approximation of da/dt ,

$$\frac{da}{dt} = \beta a + \delta a^2, \quad (13)$$

where the second term accounts for the lowest-order nonlinear effects. By shifting the phase of amplitude a , one can always make coefficient δ here real and positive. The solution of the equation reads as

$$a = \frac{\beta}{(\delta + \beta/a_0)e^{-\beta t} - \delta}, \quad (14)$$

where $a_0 = a(0)$ is an initial mode amplitude.

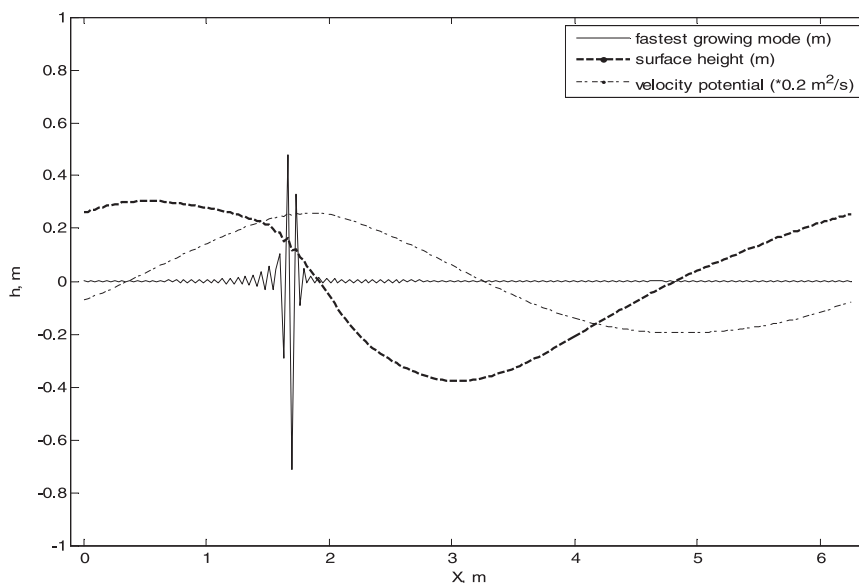


FIG. 9. The height of the surface profile (dashed), velocity potential (dashed-dotted), and the fastest growing mode (solid) vs x .

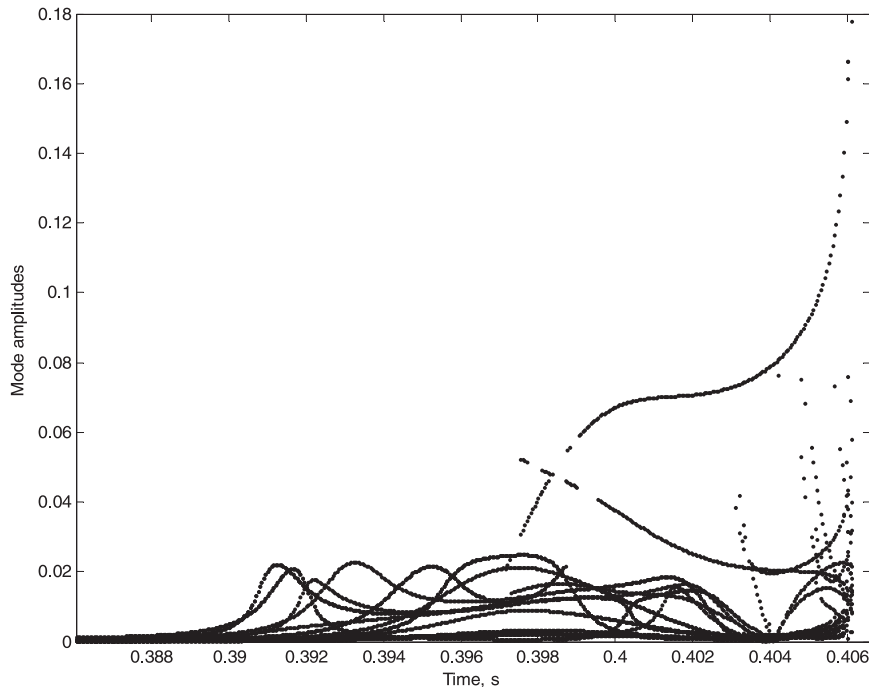


FIG. 10. Time dependence of some of the mode amplitudes at the final stage of instability development. One single mode is growing much faster than the others. (Most of the modes were removed to make visible the fastest growing one. Because of the original 400 modes are randomly sorted at each time step, removing some of them resulted in a few dropouts.)

If $a_0 > 0$, the solution is explosive; that is, it tends to infinity in a finite time. The time of explosion t_e depends relatively weakly (logarithmically) on the level of nonlinearity δ and initial amplitude a_0 : $t_e = \ln[1 + \beta/(a_0\delta)]/\beta$. On the other hand, if $a_0 < 0$, the solution tends to a finite limit. Note that similar dependence of the instability on the sign of initial perturbation was observed by Longuet-Higgins and Dommermuth (1997).

Eigenvector analysis renders some interesting aspects of the system evolution. It is easy to show that eigenvalues λ of the matrix in (12) form quadruples $(\lambda, \lambda^*, -\lambda, -\lambda^*)$, which degenerate into pairs $(\lambda, -\lambda)$ or (λ, λ^*) if λ is purely real or imaginary. It is interesting also to look into the time evolution of the eigenvalues. There are $2N = 400$ different eigenvalues altogether; they are indicated by points on the complex plane (ω, γ) , where $\omega = \text{Im}(\lambda)$ is a frequency and $\gamma = \text{Re}(\lambda)$ is an increment (see Fig. 13). Apparently, the cluster of points should be symmetric with respect to both horizontal and vertical axes. As time progresses, these eigenvalues change position on the complex plane along certain trajectories. Purely imaginary eigenvalues are located on the horizontal axis and as a result of the evolution can collide. If the two colliding eigenvalues correspond to the eigenvectors (modes) with different signs of the adiabatic invariant (different signatures using terminology of MacKay

and Saffman 1986), the eigenvalues after collision acquire real parts with different signs and leave the horizontal axis. Figure 14 shows a zoomed area around the ω axis marked by the rectangle in the Fig. 13 (time interval in Fig. 14 is slightly increased compared to Fig. 13 to better show the roots' track).

Presence of the eigenvalues with a nonzero real part does not necessarily mean instability of the wave, because its increment γ is usually small enough and evolution of

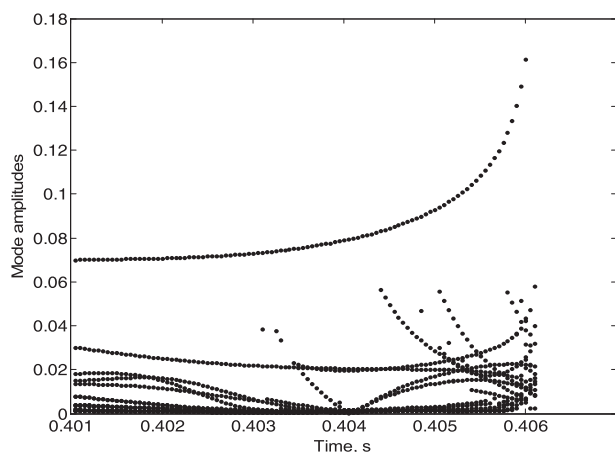
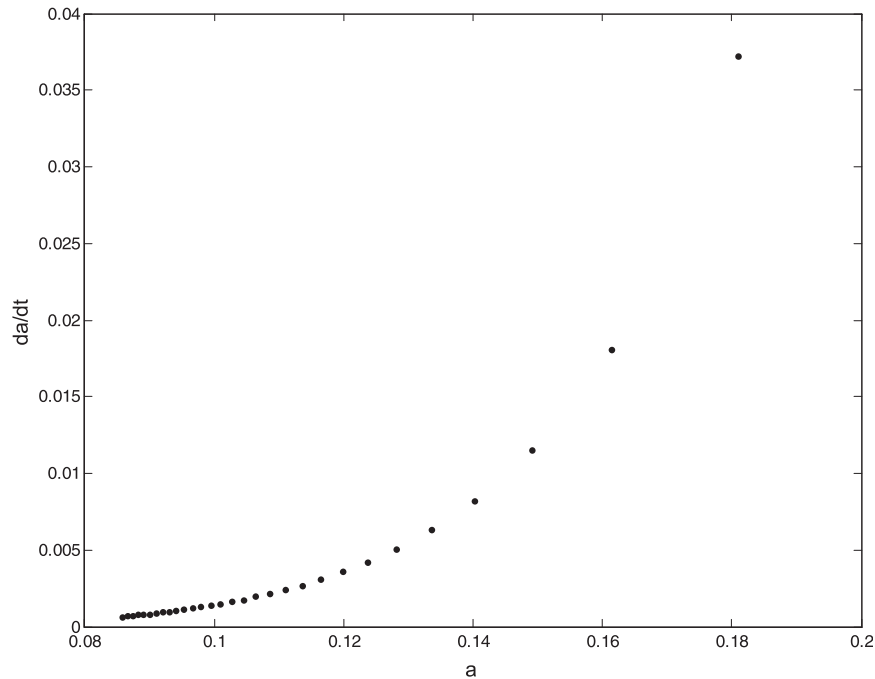


FIG. 11. As in Fig. 8, but for fewer modes and a finer time step.

FIG. 12. Numerically calculated dependence of da/dt vs a .

the wave profile does not let the instability enough time to develop. After some time, the pair of complex roots can return to the horizontal axis, collide, and become purely imaginary again; such behavior produces “instability

bubbles” (MacKay and Saffman 1986) clearly seen in Fig. 14 in the vicinity of the real axis. However, one can see in Fig. 13 that there are eigenvalues whose trajectories are directed toward the vertical γ axis. When

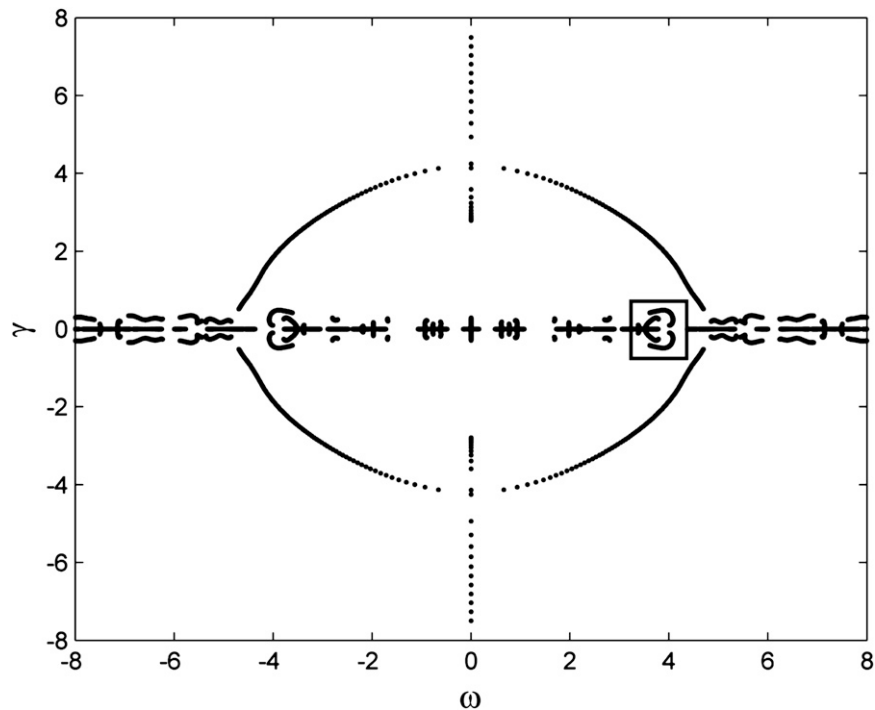


FIG. 13. Evolution of roots in a complex plane. Four roots collide at an imaginary axis, resulting in fast-growing, explosive modes.

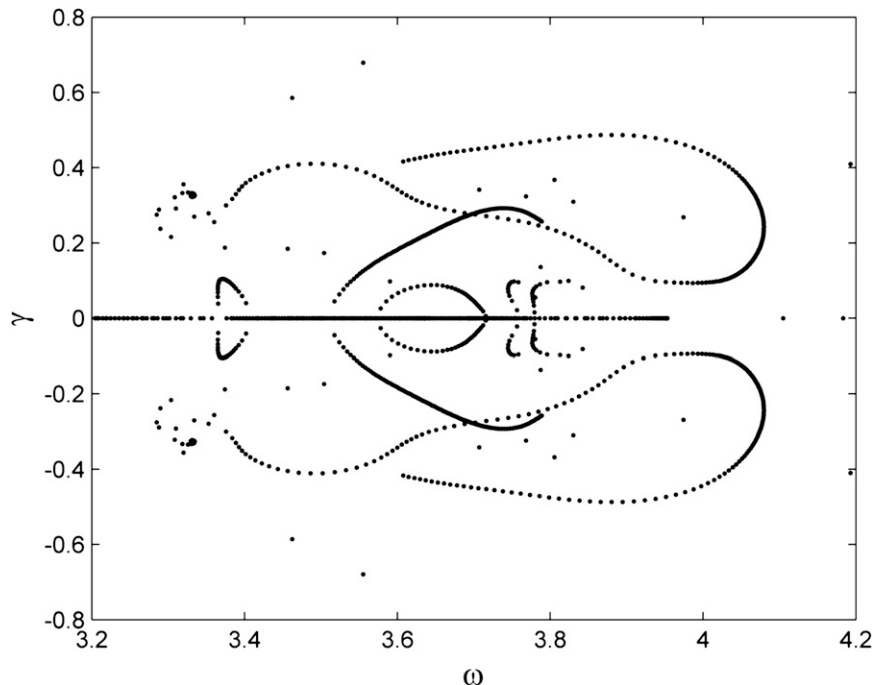


FIG. 14. Example where most of the roots are grouped around real axis, producing local loops without instability development.

they reach the vertical (incremental) axis they collide, and after the collision the pair starts to move along the axis. The mode corresponding to the eigenvalue that moves away from the origin is the fastest-growing mode considered above. It should be noted that, although collision of the eigenvalues at the incremental axis is rather typical for wave breaking, some cases of wave breaking were also observed when the eigenvalues simply moved off the horizontal axis reaching large γ but without colliding on the γ axis.

At present time, we do not have a clear physical interpretation of such root “kinematics,” but an interesting and important finding is that the explosion of a discrete Hamiltonian system [(3) and (4)] occurs because of the very fast growth of a single mode.

5. Effect of surface tension

Until now we have not accounted for surface tension, and it was assumed in (3) that $\sigma = 0$. Because of limited range of wavenumbers from $k_1 = 1 \text{ m}^{-1}$ to $k_2 = 100 \text{ m}^{-1}$ for $N = 200$, we increased the value of the surface tension T to make the parameter $k_m = (\rho g/T)^{1/2} = (g/\sigma)^{1/2}$ equal to $k_m = 50 \text{ m}^{-1}$ compared with $k_m = 370 \text{ m}^{-1}$ for clear water (this corresponds to a change of the surface tension from $T = 0.072 \text{ N m}^{-1}$ to $T = 3.9 \text{ N m}^{-1}$).

Figures 15 and 16 show the evolution of the surface power spectrum Φ_k with (lower lines) and without

(upper lines) capillary forces. Each spectrum was obtained by averaging of 300 random surface profiles with an initial condition corresponding to the k^{-3} spectrum from 1 to 50 rad m^{-1} and flat white noise spectrum for $k > 50 \text{ m}^{-1}$. The level of white noise was taken at about 0.005 of the level of the spectrum at $k = 50 \text{ m}^{-1}$. Figure 15 shows the detailed spectra after 0.01 s of wave evolution, and different panels of Fig. 16 show change of the spectrum in time. One can observe two main effects: smoothing of the steplike discontinuity of the spectrum due to nonlinear wave-wave interaction and suppression of high-frequency waves due to capillary forces. There are some oscillations of the transitional spectra; the nature of which is not quite clear, but the main features of the spectrum evolution are not surprising. Note that the energy of the system is conserved because of the Hamiltonian property of the governing equations, so the capillary wave depression is accompanied by enhancement of the longer waves at $k < 50 \text{ m}^{-1}$. This effect is obscured in Figs. 15 and 16 by a logarithmic axis scale. Despite suppression of high-frequency waves, the surface tension does not prevent development of the instability.

6. Breaking threshold

Figure 17 shows the dependence of the mean “breaking frequency” versus RMS current gradient $\partial u/\partial x = \partial^2 \varphi/\partial x^2$ calculated for the initial spectrum $\sim k^{-3}$ with random

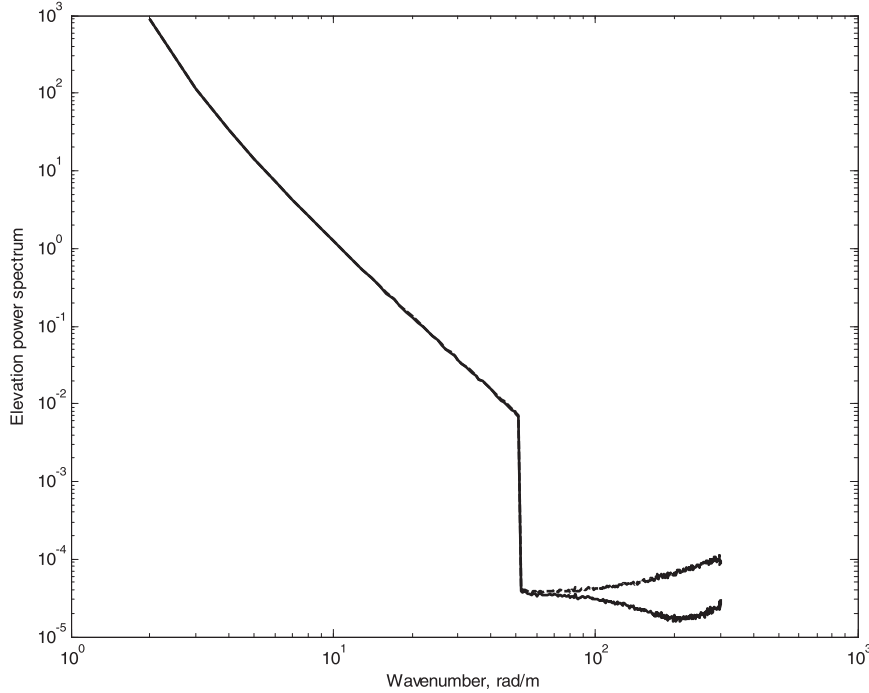


FIG. 15. Power spectra of the surface with (lower line) and without (upper line) surface tension at the very first moment of surface evolution ($t = 0.01$ s).

phases of harmonics. Breaking frequency was defined as an ensemble average of $\langle 1/T \rangle$, where T is the total time of a particular run from starting moment until breaking event (each data point in Fig. 17 was obtained by averaging of about 300 realizations of random waves). We changed RMS current gradient by changing the amplitude A of initial wave spectrum $\Phi_k = Ak^{-3}$. It is easy to see that there is a threshold: for $\sqrt{\langle (\partial u / \partial x)^2 \rangle} < 1.25 \text{ s}^{-1}$, breaking is very rare (we linearly interpolated the dependency down to the x axis), but it is growing rapidly with the increase of the amplitude of the spectrum. The corresponding threshold of RMS slope is 0.12.

It was determined experimentally by Ochi and Tsai (1983) that the criterion of wave breaking is as follows:

$$\frac{H}{gT^2} \geq 0.02, \quad (15)$$

where $H = 2a$ is the wave height, $T = 2\pi/\omega_k$ is the wave period, and k is a wavenumber. Taking into account that

$$\Omega = -\varphi_{xx} = k^2 \varphi = \frac{gk^2}{\omega_k} a, \quad (16)$$

we can represent

$$\frac{H}{gT^2} = \frac{2a\omega_k^2}{g(2\pi)^2} = \frac{2\Omega\omega_k^3}{(2\pi)^2 g^2 k^2} = \frac{1}{2\pi^2} \frac{\Omega}{\sqrt{gk}}. \quad (17)$$

Substituting here $k = 1 \text{ m}^{-1}$ and $\Omega = 1.25 \text{ Hz}$ (see Fig. 17), one finds that

$$\frac{H}{gT^2} = 0.02. \quad (18)$$

In Fig. 1 of Banner and Tian (1998), two cases are shown that correspond to very close initial steepness. Benjamin–Feir instability causes modulation which leads a steeper wave train to breaking, and a gentler wave train to recurrence. Horizontal velocities at the steepest crests for these two cases are $u = 0.94c_g$ and $u = 0.70c_g$, where c_g is the group velocity of the corresponding linear wave. Then one evaluates the horizontal velocity gradient as

$$\Omega = \frac{du}{dx} = k \frac{1}{2} \sqrt{\frac{g}{k}} \frac{u}{c_g} = \frac{1}{2} \sqrt{gk} \frac{u}{c_g}. \quad (19)$$

From Fig. 1 in Banner and Tian (1998) one can estimate $k \sim 1 \text{ m}^{-1}$ and to obtain $\Omega = 1.25 \text{ Hz}$ one must have $u/c_g \sim 0.8$, which is close to the middle of the interval of steepness for the two cases indicated above. We should take this estimate with caution because of subsequent revision of some of their results (Song and Banner 2002).

Similarly, from Fig. 11b of Baldock et al. (1996), one can estimate

$$\Omega = \frac{du}{dx} = \frac{1}{c_p} \frac{du}{dt} = \left(\frac{g}{2\pi f} \right)^{-1} \frac{du}{dt} \sim 1.3 \text{ s}^{-1}, \quad (20)$$

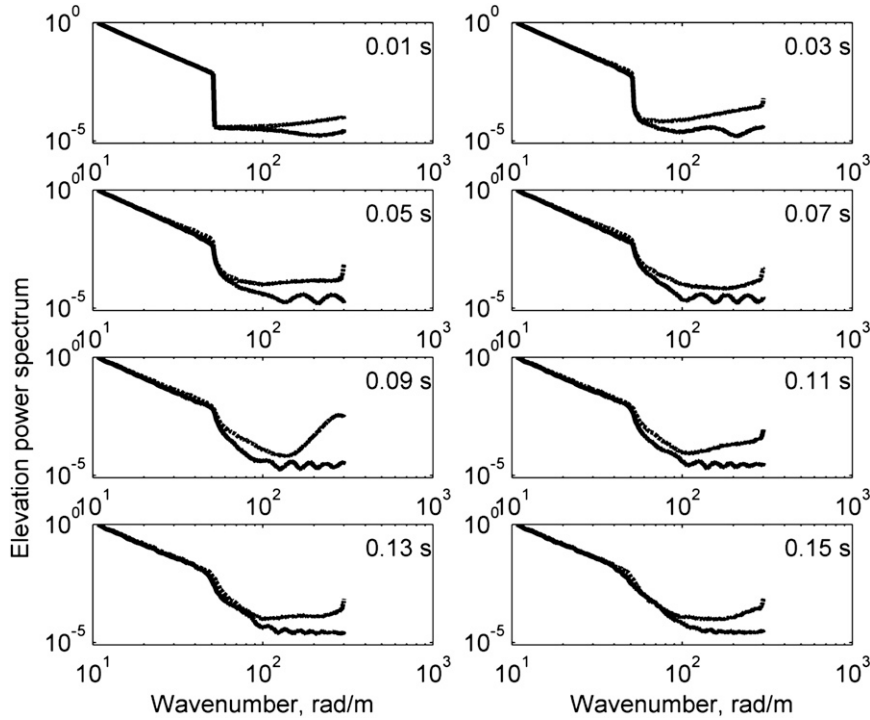


FIG. 16. Change of the power spectra in time with (lower lines) and without (upper lines) surface tension forces.

where $f = 1$ Hz (case D). This value of Ω is also close to the critical value found in our work.

In a statistical case, one has

$$\sigma = \left(\int_{k_1}^{k_2} \Phi_k dk \right)^{1/2} \quad \text{and} \quad (21)$$

$$\Omega = \langle \varphi_{xx}^2 \rangle^{1/2} = \left(g^2 \int_{k_1}^{k_2} \frac{k^4}{\omega_k^2} \Phi_k dk \right)^{1/2} \\ = \left(g \int_{k_1}^{k_2} k^3 \Phi_k dk \right)^{1/2}, \quad (22)$$

where Φ_k is the wave height spectrum. Assuming $\Phi_k = Ak^{-3}$, we obtain

$$\sigma = \frac{\Omega}{k_1 \sqrt{2gk_2}}, \quad (23)$$

where we took into account that $k_1 \ll k_2$. Significant spectral peak steepness ε is defined by Banner et al. (2000) as follows: $\varepsilon = 2\sigma k_1$. That leads us to the following dimensionless breaking criterion:

$$\varepsilon = \sqrt{\frac{2}{k_2} \int_{k_1}^{k_2} k^3 \Phi(k) dk} > \varepsilon_*. \quad (24)$$

Using $k_1 = 1 \text{ m}^{-1}$ to $k_2 = 100 \text{ m}^{-1}$, the parameters used in our numerical simulations, one finds that $\varepsilon_* = 0.056$. The threshold value suggested by Banner et al. (2000) is $\varepsilon_* = 0.055$. Taking into account the highly idealized model used in our numerical simulations, the near coincidence of the appropriate numbers above should be considered as accidental; however, their closeness indicates that the suggested criterion of wave breaking,

$$\Omega > \Omega_*, \quad (25)$$

is consistent with the data of the other researches.

7. Conclusions

We can suggest the following scenario for wave breaking in a random field of surface gravity waves: The whole wave ensemble generates zones of convergence of surface currents. The waves with lengths less than the size of the convergence zone start to contract. If the parameter $\Omega = \partial u / \partial x$ for the convergence zone, initial amplitude of the contracting wave, and duration of the existence of the convergence zone are large enough, the steepness of the wave will exceed critical value and a breaking event will take place. The breaking event is not necessarily related to a particular wave from the background, which creates a convergent current, and in this sense it is not

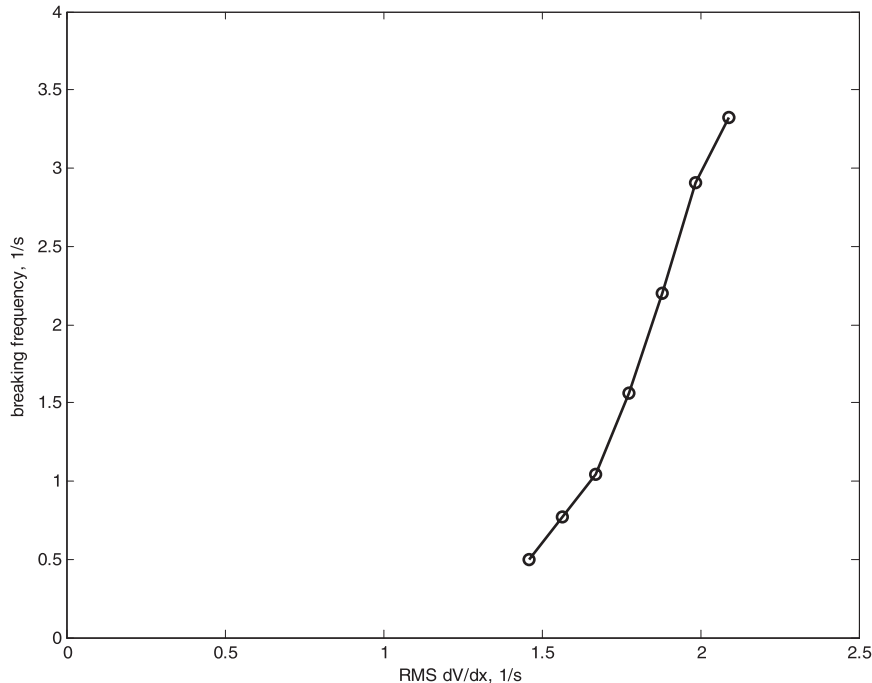


FIG. 17. The dependence of the averaged breaking frequency on mean surface current gradient.

quite accurate to say that a particular wave from the ensemble of longer waves breaks; the breaking event is rather a collective effect of an ensemble of longer waves, which leads to the contraction and breaking of shorter waves. For power-law surface elevation spectrum $\Phi_k = Ak^{-n}$ where $n > 4$, the dominant contribution to Ω comes from the low-frequency end of the spectrum [see (22)]; for $n < 4$, it is due to the high-frequency end. If the contracting wave that eventually breaks is long enough, the plunging breaker will be generated; if it is sufficiently short so that surface tension becomes important, it will be a spilling breaker.

The zones of divergence of surface currents play opposite role and have a tendency to smooth the surface. This conforms to the casual observations that the back side of waves is usually much calmer than their front side.

Acknowledgments. We are thankful to Alexander Babanin and anonymous reviewers for numerous very valuable corrections and suggestions.

APPENDIX

Dependence on Number of Points

Our model Hamiltonian (3) describes a discrete system that fundamentally differs from a continuous system by a finite number of degrees of freedom. This appendix is devoted to study how critical is the presence of the

highest, most oscillating mode for the development of the instability.

To clarify this issue we conducted a series of the calculations for a different number of points from $N = 200$ to $N = 600$ for the three different situations:

- 1) the original discrete Hamiltonian system;
- 2) the discrete Hamiltonian system with capillary forces; and
- 3) the original Hamiltonian system with low-pass filtering applied at each time step, where the filter damps all spatial harmonics with $k > 80 \text{ m}^{-1}$ (the highest wavenumber for $N = 200$ is $k_2 = 100 \text{ m}^{-1}$).

Figure A1 shows the dependence of the mean breaking frequency (see section 7 for the definition of this parameter) versus the maximum wavenumber for all three versions. We can see that the breaking frequency depends on the highest wavenumber for the original Hamiltonian, but accounting for the surface tension (the surface tension corresponds to $k_m = 50 \text{ m}^{-1}$) results in a saturation of the dependence. The process of wave breaking becomes weakly dependent on (or independent of) the number of points if capillary forces are introduced. The low-pass filtering results in complete independence of the breaking frequency on the number of points. Nevertheless, one can see that the instability develops even in this case. Moreover, the cases with the same initial condition (i.e., the same amplitudes and phases of the

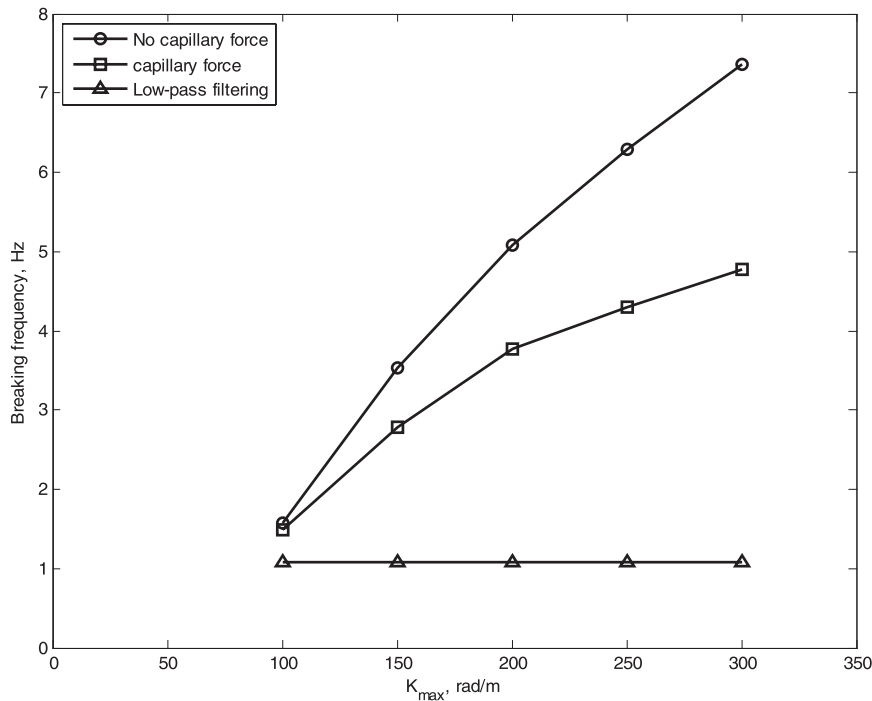


FIG. A1. Breaking frequency vs maximal wavenumber (numerically equal to $\frac{1}{2}$ of point number for surface period of 6.28 m). Circles correspond to motion without capillary forces, squares correspond with the model surface tension, and triangles correspond with low-pass filtering at each time step.

harmonics), but with a different number of points evolve to the same final state.

Figure A2 shows an example of such system evolution for a different number of points. The area marked by the

rectangle is shown in Fig. A3. It illustrates the insignificance in the difference between unstable modes despite a complete absence of high-frequency harmonics in the cases with $N = 200$ and $N = 600$. We see that even

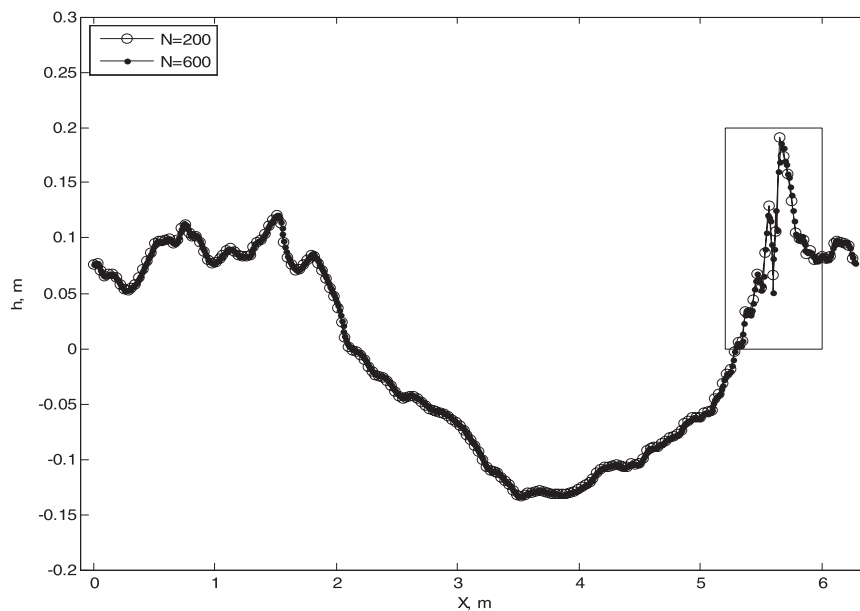


FIG. A2. Comparison of the solutions with a different number of points at a final time step. Low-pass filtering is applied at each time step.

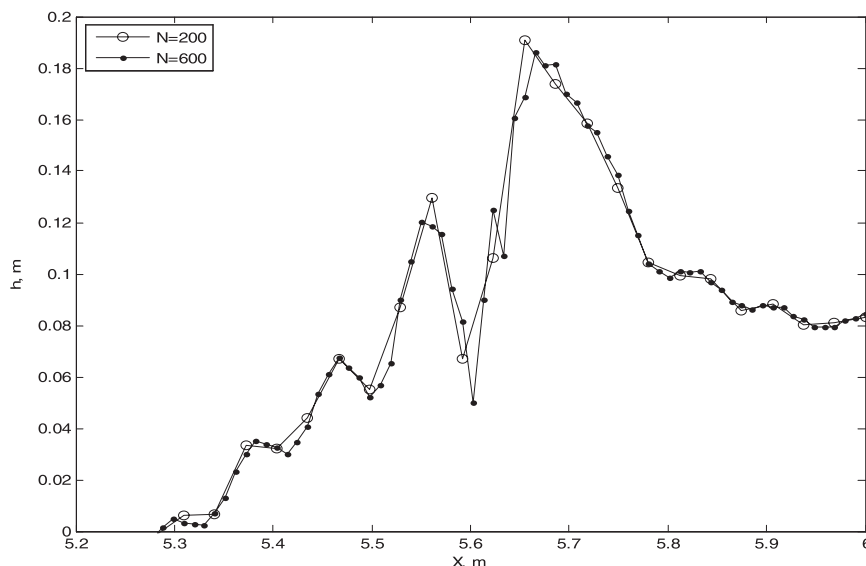


FIG. A3. Zoomed area, indicated by the rectangle in Fig. A2.

fine details of the system evolution are preserved despite filtering. This observation supports our claim that the observed instability is not a numerical effect related to the finite-dimensional approximation of the system but is of a physical origin.

REFERENCES

- Babanin, A., D. Chalikov, I. Young, and I. Savelyev, 2007: Predicting the breaking onset of surface water waves. *Geophys. Res. Lett.*, **34**, L07605, doi:10.1029/2006GL029135.
- , —, —, and —, 2010: Numerical and laboratory investigation of breaking of steep two-dimensional waves in deep water. *J. Fluid Mech.*, **644**, 433–463, doi:10.1017/S002211200999245X.
- Baldock, T. E., C. Swan, and P. H. Taylor, 1996: A laboratory study of nonlinear surface waves on water. *Philos. Trans. Roy. Soc. London*, **354A**, 649–676.
- Banner, M. L., and D. H. Peregrine, 1993: Wave breaking in deep water. *Annu. Rev. Fluid Mech.*, **25**, 373–379.
- , and X. Tian, 1998: On the determination of the onset of breaking for modulating surface gravity water waves. *J. Fluid Mech.*, **367**, 107–137.
- , A. V. Babanin, and I. R. Young, 2000: Breaking probability for dominant waves on the sea surface. *J. Phys. Oceanogr.*, **30**, 3145–3160.
- , J. R. Gemmrich, and D. M. Farmer, 2002: Multiscale measurements of ocean breaking probability. *J. Phys. Oceanogr.*, **32**, 3364–3375.
- Bonmarin, P., 1989: Geometric properties of deep-water breaking waves. *J. Fluid Mech.*, **209**, 405–433.
- Caulliez, G., 2002: Self-similarity of near-breaking short gravity wind waves. *Phys. Fluids*, **14**, 2917–2920.
- Chalikov, D., and D. Sheinin, 1998: Direct modeling of one-dimensional nonlinear potential waves. *Nonlinear Ocean Waves*, W. Perrie, Ed., Advances in Fluid Mechanics, Vol. 17, Computational Mechanics Publications, 207–258.
- , and —, 2005: Modeling extreme waves based on equations of potential flow with a free surface. *J. Comput. Phys.*, **210**, 247–273, doi:10.1016/j.jcp.2005.04.008.
- Dold, J. W., 1992: An efficient surface-integral algorithm applied to unsteady gravity waves. *J. Comput. Phys.*, **103**, 90–115.
- Dommermuth, D. G., D. K. P. Yue, W. M. Lin, R. J. Rapp, E. S. Chan, and W. K. Melville, 1988: Deep-water plunging breakers: A comparison between potential theory and experiments. *J. Fluid Mech.*, **189**, 423–442.
- Duncan, J. H., 2001: Spilling breakers. *Annu. Rev. Fluid Mech.*, **33**, 519–547.
- Gemmrich, J. R., 2010: Strong turbulence in the wave crest region. *J. Phys. Oceanogr.*, **40**, 583–595.
- , and D. M. Farmer, 2004: Near surface turbulence in the presence of breaking waves. *J. Phys. Oceanogr.*, **34**, 1067–1086.
- , M. L. Banner, and C. Garrett, 2008: Spectrally resolved energy dissipation rate and momentum flux of breaking waves. *J. Phys. Oceanogr.*, **38**, 1296–1312.
- Griffin, O. M., R. D. Peltzer, and H. T. Wang, 1996: Kinematic and dynamic evolution of deep water breaking waves. *J. Geophys. Res.*, **101** (C7), 16 515–16 531.
- Holthuijsen, L. H., and T. H. C. Herbers, 1986: Statistics of breaking waves observed as whitecaps in the open sea. *J. Phys. Oceanogr.*, **16**, 290–297.
- Iafrati, A., 2009: Numerical study of the effects of breaking intensity on wave breaking flows. *J. Fluid Mech.*, **622**, 371–411, doi:10.1017/S0022112008005302.
- Louquet-Higgins, M. S., 1988: Mechanisms of wave breaking in deep water. *Sea Surface Sound*, B. R. Kerman, Ed., Springer, 1–30.
- , and E. D. Cokelet, 1976: The deformation of steep surface waves on water. I: A numerical method for computation. *Proc. Roy. Soc. London*, **350A**, 1–26.
- , and —, 1978: The deformation of steep surface waves on water. II: Growth of normal-mode instabilities. *Proc. Roy. Soc. London*, **364A**, 1–28.
- , and D. G. Dommermuth, 1997: Crest instabilities of gravity waves. Part 3. Nonlinear development and breaking. *J. Fluid Mech.*, **336**, 33–50.

- MacKay, R. S., and P. G. Saffman, 1986: Stability of water waves. *Proc. Roy. Soc. London*, **406A**, 115–125.
- Melville, W. K., 1982: The instability and breaking of deep-water waves. *J. Fluid Mech.*, **115**, 165–185.
- , 1996: The role of surface-wave breaking in air-sea interaction. *Annu. Rev. Fluid Mech.*, **28**, 279–321.
- , and R. J. Rapp, 1988: The surface velocity field in steep and breaking waves. *J. Fluid Mech.*, **189**, 1–22.
- Nepf, N. M., C. H. Wu, and E. S. Chan, 1998: A comparison of two- and three-dimensional wave breaking. *J. Phys. Oceanogr.*, **28**, 1496–1510.
- Ochi, M. K., and C.-H. Tsai, 1983: Prediction of occurrence of breaking waves in deep water. *J. Phys. Oceanogr.*, **13**, 2008–2019.
- Perlin, M., J. He, and L. Bernal, 1996: An experimental study of deep water plunging breakers. *Phys. Fluids*, **8**, 2365–2374.
- Rapp, R. J., and W. K. Melville, 1990: Laboratory measurements of deep-water breaking waves. *Philos. Trans. Roy. Soc. London*, **331**, 735–800.
- Skyner, D., 1996: A comparison of numerical predictions and experimental measurements of the internal kinematics of a deep-water plunging wave. *J. Fluid Mech.*, **315**, 51–64.
- Song, C., and A. I. Sirviente, 2004: A numerical study of breaking waves. *Phys. Fluids*, **16**, 2649–2667.
- Song, J.-B., and M. L. Banner, 2002: On determining the onset and strength of breaking for deep water waves. Part I: Unforced irrotational wave groups. *J. Phys. Oceanogr.*, **32**, 2541–2558.
- Stansell, P., and C. MacFarlane, 2002: Experimental investigation of wave breaking criteria based on wave phase speeds. *J. Phys. Oceanogr.*, **32**, 1269–1283.
- Weissman, M. A., S. S. Atakturk, and K. B. Katsaros, 1984: Detection of breaking events in a wind-generated wave field. *J. Phys. Oceanogr.*, **14**, 1608–1619.
- Wu, C. H., and H. M. Nepf, 2002: Breaking criteria and energy losses for three-dimensional wave breaking. *J. Geophys. Res.*, **107**, 3177, doi:10.1029/2001JC001077.
- Xu, D., P. A. Hwang, and J. Wu, 1986: Breaking of wind-generated waves. *J. Phys. Oceanogr.*, **16**, 2172–2178.